# Combined nanoindentation and SEM imaging for phase quantification and creep prediction of cementitious materials

Imane Bekrine, Benoit Hilloulin, Ahmed Loukili

Materials & Design 250 (2025) 113607

Contents lists available at ScienceDirect

Materials & Design

journal homepage: www.elsevier.com/locate/matdes

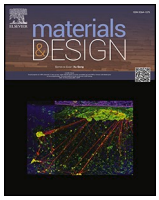

# Combined nanoindentation and SEM imaging for phase quantification and creep prediction of cementitious materials

Imane Bekrine, Benoit Hilloulin *, Ahmed Loukili

*Nantes Université, Ecole Centrale Nantes, CNRS, GeM, UMR 6183, F-44000 Nantes, France*

ARTICLE INFO

*Keywords:*
Nanoindentation
Microstructure [B]
Calcium-silicate-hydrate (C–S–H) [B]
Micromechanics [C]
Creep

ABSTRACT

The present article introduces a novel and rapid method for processing nanoindentation data using SEM image analysis, called Auto-NI-SEM (Automatic NanoIndentation-Scanning Electron Microscopy). The originality of the method lies in the exploitation of micromechanical data, coupled with image analysis, by developing a suitable automatic deconvolution method. The method leads to a rapid phase quantification of cement paste phases along with their elastic and viscoelastic properties, essential for accurate prediction of macroscopic properties. The results were validated on cement pastes with different water-to-cement (w/c) ratios. Furthermore, the method was found to be reliable for the detection of minor phases, such as for portlandite in low water-to-cement ratios cement pastes, whose volume fractions are in line with those measured by thermogravimetric analysis. Finally, the refined properties helped to accurately predict the cement pastes creep using an analytical homogenization scheme, which was confirmed by microindentation measurements.

## 1. Introduction

In order to achieve a comprehensive understanding of the macroscopic behavior of cementitious materials, their microstructural features need to be well controlled and monitored, especially their binding phase properties, i.e. hydration products [1]. In this aim, different experimental techniques were employed to investigate the binding phase properties, primarily composed of calcium silicate hydrates (CSH) and calcium hydroxide (CH/portlandite), at both the microscale and nanoscale. These techniques include SEM [2,3] and nanoindentation [4]. On one hand, imaging techniques such as SEM were used to qualitatively and quantitatively characterize the microstructures of cementitious materials for various uses [5,6]. For example, gray level analysis of the images allows for quantification of some specific phases of hardened cementitious materials, their water-to-cement ratio and their degree of hydration [7–11], as well as the degree of hydration of mineral additions, e.g. slag, with additional chemical analyses [12]. SEM images were also used to assess the composition of cement pastes, even the complex ones, as training inputs for machine learning models [13], or alternatively as a framework to enable their utilization alongside EDS hypermaps, in order to analyze paste compositions and determine the particle shapes and their spatial distribution in complex microstructures [14,15].

On the other hand, nanoindentation has proved to be a useful technique in assessing the micromechanical properties of binding phase components, notably CSH and portlandite [16]. Application of small loads (1 – 10 mN) leads to hundreds of nanometer penetration depths; given the characteristic size of cement paste heterogeneities (500 nm – 10 μm), several phases may be indented at the same time. To overcome this limitation, grid nanoindentation was introduced to statistically analyze and determine the phase properties [17]; furthermore, numerous deconvolution algorithms have been introduced so as to cluster indentation data into groups of individual phases. For instance, the least square estimate (LSE) algorithm can serve to fit the probability density function (PDF) or cumulative distribution function (CDF) of nanoindentation data by minimizing the error between theoretical and experimental data; however, it has the disadvantage of converging to a local optimum [18]. Expectation-Maximization algorithm-based models, such as Gaussian Mixture Models (GMM), have thus been introduced within the last decade to cluster nanoindentation data and search for global optima [19,20]. Zhen *et al.* [21] compared three deconvolution methods, revealing the influence of the number of indents and indentation method parameters on the outputs, thus substantiating the need for a reliable and rapid data deconvolution method. Nonetheless, the validity of these methods is still being questioned since the determined clusters may not actually represent pure single phases of cementitious materials.

* Corresponding author.
*E-mail address:* benoit.hilloulin@ec-nantes.fr (B. Hilloulin).

https://doi.org/10.1016/j.matdes.2025.113607
Received 5 June 2024; Received in revised form 24 December 2024; Accepted 10 January 2025
Available online 11 January 2025

**Nomenclature**

*Summary of abbreviations: Materials and pastes' phases*

| | |
|---|---|
| OPC | Ordinary Portland cement |
| CSH | Calcium Silicate Hydrate |
| CASH | Calcium Alumino-Silicate Hydrate |
| LD CSH | Low-density CSH |
| HD CSH | High-density CSH |
| UHD CSH | Ultra-high-density CSH |
| CH | Portlandite/calcium hydroxide |
| UC | Unhydrated cement |

*Experimental and numerical techniques*

| | |
|---|---|
| SEM | Scanning electron microscopy |
| EDS | Energy dispersive spectroscopy |
| BSE | Backscattered electrons |
| MIP | Mercury intrusion porosity |
| TGA | Thermogravimetric analysis |
| GMM | Gaussian Mixture Model |
| PDF | Probability density function |
| Auto-NI-SEM | Automatic NanoIndentation-Scanning Electron Microscopy |

For this reason, deconvolution results have been combined with other measurement techniques in order to refine pure characterization of multiphase materials. For metallic materials, nanoindentation is often combined to electron backscatter diffraction (EBSD) in order to analyze their microstructure [22,23]. In other cases, it can be useful to chemically investigate indented areas using energy-dispersive spectroscopy (EDS). Through an EDS analysis of nanoindents-comparable micro-volumes [20], Chen *et al.* [24] were indeed able to prove the formation of CSH/CH nanocomposites being intimately intermixed in low water-to-cement ratio cement pastes. Wilson *et al.* [25] showed the impact of OPC replacement by natural pozzolan on the paste micromechanical properties, in particular with portlandite transformation to the CASH phase. Abdallah *et al.* [26] sought an explanation for the physical origin of the dispersion observed on macroscopic measurements of Young's modulus in carbonate rocks, even those featuring similar porosities, in accordance with the relative fractions of mineral phases and their mechanical properties. Wei *et al.* [27] demonstrated that inner products around unhydrated slag particles contained more magnesium (Mg) in their composition yet did not differ from OPC inner products. Hilloulin *et al.* [28] determined the γ-irradiated cement paste properties in mortars using coupled microindentation and 3D microscope observations of the indented areas. Microscopic images of hot-pressed lignins coupled to nanoindentation measurements enabled exclusion of measurements affected by porosity [29]. Scanning Electron Microscope (SEM) images were also used to provide additional information on the elastic properties of the indented phases [30,31]. Effective exploitation of such coupling needs to be implemented to refine and reduce uncertainty on the elastic and viscoelastic properties of pure cement paste phases' measured by nanoindentation. Creep of cementitious materials at the micro-scale has also been measured using micro-pillar and micro-cantilever beam tests. These methods are particularly effective for capturing the short-term creep of cementitious materials. For instance, Gan *et al.* [32] utilized miniaturized cement paste cantilever beams for micro-bending tests, demonstrating that these tests complement indentation-based methods, which are better suited for long-term creep assessments. Similarly, Guo and Wei [33] conducted compressive indentation tests on micropillars, capturing the short-term creep behavior of CSH phases. However, these methods, while valuable at the micro-scale, do not provide insights into the influence of individual phases on the overall viscoelastic properties of cementitious materials.

The exploitation of information at this scale may help to not only understand some macroscopic observations on concrete, but also predict their behavior at higher scales. Comprehensive use of micromechanical properties in order to simulate the meso/macroscale properties of concrete was reported in the literature. For instance, Su *et al.* [34] developed an innovative multiscale model to simulate the effect of a wide range of aggregates and ITZ configurations on the creep of concrete at the mesoscale. Another hierarchical creep model was introduced taking into consideration the microstructural evolution of pastes during hydration [35]. Multiple other works predicted creep at meso/macro scale using creep modulus of cement pastes' individual phases, with volume fractions issued from multiple other experimental techniques, such as thermogravimetry and SEM image analysis [36–38]. However, to the best of the authors' knowledge, the nanoindentation-determined composition of cement pastes was never directly used as input data for analytical homogenization models predicting creep.

In the present study, a novel simple method for nanoindentation data processing is proposed, enabling pure phase quantification in cementitious materials and micromechanical properties refinement. To this end, numerical clustering of nanoindentation data using the GMM algorithm was coupled to grayscale analysis of SEM images in the indented areas. First, a zoom on the functioning of the proposed method will be demonstrated (section 3.1) on one selected paste: OPC-0.23 at 28 days. The results are similar for all studied pastes with w/c ratio ranging from 0.23 to 0.4. Then, these results for all studied samples are analyzed and discussed in sections 3.2 and 3.3. In section 3.2, the proposed method will be employed to determine the composition of cement pastes with various water-to-cement ratios, along with the refined micromechanical properties of the individual phases and thereby re-establish the influence of water-to-cement ratio and gel porosity on CSH elastic and viscoelastic properties. Finally in section 3.3, the phases properties and volume fractions will be used as input data to an analytical homogenization model for the pastes creep prediction.

## 2. Materials and methods

### 2.1. Materials and sample preparation

Four ordinary Portland cement pastes with water-to-cement (w/c) ratios of 0.23, 0.3, 0.35 and 0.4 were prepared using CEM I 52.5 N, tap water and polycarboxylic superplasticizer when needed. The cement has a density and specific area of 3.15 and 3979 $cm^2/g$, respectively. Its chemical composition is detailed in Table 1, and its mineral composition calculated using Bogue's formula is: 68 % alite, 10 % belite, 9 % aluminate, and 7 % ferrite. The pastes were named after their water-to-cement ratio.

Mixing was carried out using a bowl mixer, and the samples were compacted in two equal layers on a vibrating table into prismatic molds measuring $4 \times 4 \times 16$ $cm^3$. For each layer, compaction was assumed to be complete when no significant amount of air bubbles escaped from the surface. After 24 h of curing under sealed conditions in an air-conditioned room at 20 °C and 90 % RH, the specimens were demolded and cured in lime-saturated water until the age of 28 days.

At 28 days, 1–2 cm cubes were sawn 1 cm away from the sample edges, and their hydration was stopped using 99.8 % isopropanol. The cubes were used for mercury porosimetry testing, nanoindentation and SEM imaging. As the viscoelastic properties of cement pastes are influenced by their internal relative humidity, as well as that of the chamber during indentation tests [39–43], all samples were dried in the oven at 40 °C then preconditioned at a controlled relative humidity of 65 % ± 5 %. The tests were then performed under these same relative humidity conditions. Thin slices of hardened cement paste were crushed to 80 μm after sieving to serve during thermogravimetric testing.

**Table 1**
Chemical composition (mass%) of the cement used in this study. LOI = loss on ignition.

| $SiO_2$ | $Al_2O_3$ | $Fe_2O_3$ | CaO | MgO | $SO_3$ | $K_2O$ | $Na_2O$ | $P_2O_5$ | $Cl^-$ | $S^{2-}$ | LOI |
|---|---|---|---|---|---|---|---|---|---|---|---|
| 20.4 | 4.4 | 2.3 | 64.0 | 3.9 | 2.9 | 0.66 | 0.15 | 0.1 | 0.02 | <0.02 | 1.2 |

### 2.2. Experimental testing

#### 2.2.1. Thermogravimetric analysis (TGA)

A NETZSCH microbalance was used to perform the thermal analysis of the pastes, with $N_2$ as the purging gas at a rate of 60 mL/min. 50 ± 5 mg of crushed powder were placed in alumina crucibles and subjected to temperatures rising from 20 °C to 1000 °C, at a heating rate of 10 °C per minute; the main objective being to quantify the volume fraction of portlandite in the different cement pastes in order to validate the proposed coupling method. The decomposition of portlandite due to water evaporation occurs at temperatures ranging approximately from 400 °C to 550 °C, and the weight loss in this temperature range, determined according to Marsh's tangential method [44], is used to calculate the volume fraction of portlandite in the paste as detailed in [45].

#### 2.2.2. Mercury intrusion porosimetry (MIP)

Porosity measurements were performed on cement pastes by means of mercury intrusion porosimetry (MIP) using a Micromeritics AutoPore IV porosimeter. Each sample was first placed in a low-pressure chamber, which had initially been evacuated and then injected with mercury up to a pressure of around 200 kPa. Afterwards, the sample was moved inside the high-pressure chamber, where mercury was incrementally injected to reach a maximum pressure of nearly 414 MPa.

#### 2.2.3. Microindentation testing

The creep modulus of the different pastes was determined using microindentation tests, via grids of 5 by 5 indents, spaced by 500 μm under a load controlled mode of a maximum force 2 N, held constant for 60 s. Using the same procedure that will be described in section 2.2.5 for creep modulus calculation at each indent, the creep modulus of the paste was obtained by averaging the obtained 25 values; which will be referred to as $C_{exp}$ (for experimental creep modulus) in the rest of the manuscript.

#### 2.2.4. SEM-BSE imaging

The images were captured via the BSE mode of a JEOL JSM-6060LA scanning electron microscope, at a 20 kV accelerating voltage, 5 mm working distance and 3000× magnification. Image dimensions were 1280 × 960 pixels, leading to a resolution of 33.33 nm/pixel. This magnification level was chosen as a compromise to accommodate both the precision allowing indent observation and the time required to reconstruct a BSE image of the entire indented area by merging all BSE images. Imaging was performed under partial vacuum (60 Pa) to avoid sample coating and excessive drying. For each paste, 100 images (10 × 10) were taken with an overlap between images of about 20 %; stitching then flied on Fiji software [46], thus leading to an image of approximately 9600 × 6400 pixels.

#### 2.2.5. Nanoindentation set-up

Prior to testing, the 1–2 cm cubes were impregnated in resin and polished initially using SiC papers with decreasing particle size (500, 1200, 2000, 4000), then diamond pastes (3 μm and 1 μm) on silk discs for fine polishing. The samples were carefully cleaned in an ultrasonic bath after each polishing step, in order to eliminate any remaining suspensions and surface debris. The final surface root-mean-square roughness on all samples was assessed using the Scanning Probe Microscopy mode of the nanoindenter, and was found to be lower than 50 nm.

Nanoindentation was carried out using a Berkovich nanoindenter over a grid of 31 × 20 indents, evenly spaced by 10 μm, which made it a representative indented surface covering 300 × 190 $\mu m^2$. This spacing was chosen to balance measurement accuracy, avoid overlapping effects between successive indents, and limit the duration of the nanoindentation test, all while covering a representative area of the paste. The loading function is described in Figure 1, and consists of 3 phases: a loading phase during 5 s until maximum load $P_{max}$ = 2 mN, a holding phase of 60 s in order to measure creep, and an unloading phase of 5 s. This holding time was selected to be short enough to minimize the effects of thermal drift, while also being tested and proven in prior studies [25,47,48] to be sufficiently long to capture creep, a finding that will be verified later. Typical load-penetration depth curves are shown in Figure 2. Notably, non-creeping components, such as portlandite and unhydrated cement particles, also exhibit noticeable time-dependent deformation. This observation, consistent with findings in previous studies, may result from subtle viscoelastic effects or measurement artifacts at very small scales. For portlandite, its nanoscale intermixing with CSH, as reported by Chen *et al.* [24], could explain higher time-dependent deformations observed in nanoindentation tests.

The necessary calibrations of the machine were performed, including the tip-to-optic, the tip area function and thermal drift calibrations. In addition, the thermal drift was accounted for in real-time during each test then corrected to ensure a reliable measurement of creep.

According to Oliver and Pharr's approach [49], the indentation modulus $M$, Young's modulus $E$ and hardness $H$ can be calculated as follows:

$$M = \frac{1}{2}\sqrt{\frac{\pi}{A_c}}S \tag{1}$$

$$\frac{1}{M} = \frac{1-\nu^2}{E} + \frac{1-\nu_{ind}^2}{E_{ind}} \tag{2}$$

$$H = \frac{P_{max}}{A_c} \tag{3}$$

where: $A_c$ is the projected area between the tip and the indented material; $\nu$ is the material's Poisson's ratio (which equals 0.24 for cement paste [50]); and $\nu_{ind} = 0.07$ and $E_{ind} = 1141GPa$ are respectively the Poisson's ratio and elastic modulus of the diamond indenter.

As regards viscoelastic properties, the penetration depth during the creep period is fitted as a logarithmic function in the form $\Delta h(t) = x_1 ln(1 + x_2 t)$, where $x_1$ and $x_2$ are the fitting parameters related to contact creep modulus $C$ and characteristic time $\tau$ resp. by Equations (6) and (7). The characteristic time was calculated to confirm that the

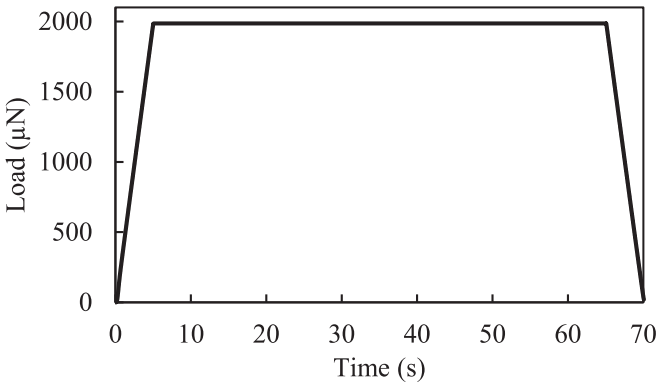


**Figure 1.** Nanoindentation loading function.

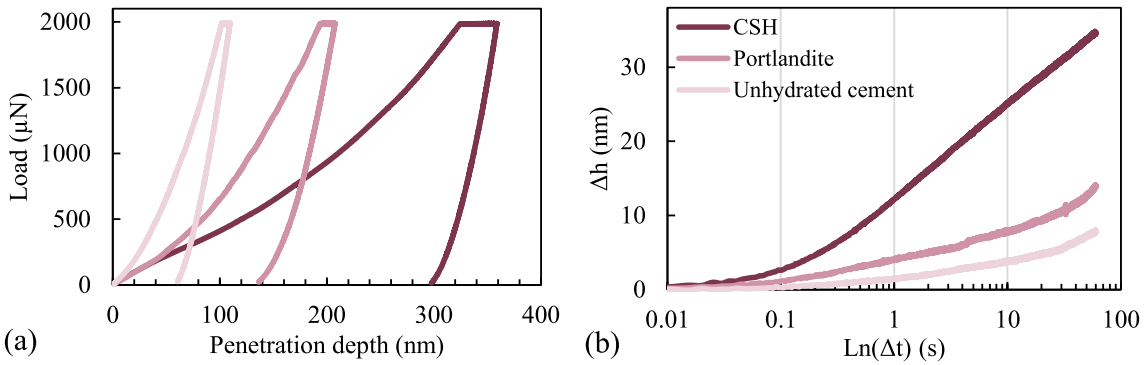


**Figure 2.** (a) Typical load-penetration depth curves of CSH, portlandite and unhydrated cement, (b) their penetration depth curves during creep.

holding time used is sufficient to capture long-term creep, as it reflects the time required to shift from a volumetric response of the material under the applied load to the long-term creep. For all the studied samples, $\tau = 0.35 \pm 0.38$ s $\ll 60$ s. The standard deviation is relatively higher than the mean value because of a small amount of outlier points with higher characteristic time values.

$$C = \frac{P_{max}}{2x_1}\sqrt{\frac{\pi}{A_c}} \tag{4}$$

$$\tau = \frac{1}{x_2} \tag{5}$$

Vandamme and Ulm [51] proved the suitability of the logarithmic fit compared to power fit of the penetration depth during creep measured by nanoindentation. In addition, logarithmic time-dependence of the creep compliance rate requires the knowledge of one parameter only ($\dot{L}(t) = \frac{1}{Ct}; C = \frac{P_{max}}{2a_U x_1}$), while the power fit requires two parameters ($\dot{L}(t) = bt^{a-1}$). They demonstrated that the contact creep moduli of the phases assessed by nanoindentation can be homogenized to well represent the uniaxial creep of concrete. Later on, Zhang *et al.* [52] showed that contact creep modulus assessed by means of microindentation is representative of concrete modulus. The use of nanoindentation in this study aims to understand the microscopic contributions of the different phases to the creep behavior of the paste, mainly for further application on the effect of mineral additions.

### 2.3. Phase inference methods

#### 2.3.1. GMM deconvolution of nanoindentation results

The indents were assigned to phases using a Gaussian Mixture Model (GMM) by assuming a total distribution $x=(E,H)$ of elastic properties composed of elastic modulus $E$ and $H$. $x$ is assumed to be a mixture of N individual phases (or clusters) of Gaussian distributions, whose probability density function is given in Eq. (6), with the individual distributions provided in Eq. (7). Bayesian Information Criterion (BIC) was used to determine the number of clusters N (whereby BIC is minimized for N).

Identifying the characteristic cluster parameters entails resolving the maximization problem expressed in Eq. (8) by means of the Expectation-Maximization (EM) algorithm.

$$p(x) = \sum_{k=1}^{N} \pi_k N(x|\mu_k, \Sigma_k); \sum_{k=1}^{N} \pi_k = 1 \tag{6}$$

$$N(x|\mu, \Sigma) = \frac{1}{\sqrt{\det(2\pi\Sigma)}} e^{-\frac{1}{2}(x-\mu)\Sigma^{-1}(x-\mu)} \tag{7}$$

$$max(ln(\prod_{l=1}^{M} p(x_l))) = max(\sum_{l=1}^{M} ln\left(\sum_{k=1}^{N} \pi_k N(x|\mu_k, \Sigma_k)\right) \tag{8}$$

where $\pi_k$, $\mu_k$ and $\Sigma_k$ are respectively the weighting coefficient, mean value and covariance of the $k^{th}$ component, and M is the number of indents.

Prior to GMM clustering, indents with E > 120 GPa or H > 12 GPa were excluded due to the sensitivity of the algorithm to singular points.

During a final step, the contact creep modulus $C$ is calculated based on the clusters defined by GMM. This procedure has been accurately described in [53].

#### 2.3.2. SEM images analysis

Square images of 80 × 80 pixels (corresponding to 2.67 × 2.67 μm$^2$, i.e. slightly larger than the biggest indent imprint) were extracted from BSE images around each indent. Since all indents could not be located on the images, a dedicated procedure was established to infer the indent position based on the indent matrix corner positions. Thanks to the high image resolution, a grayscale analysis could be performed on every single image. The mean grayscale value $m$ and standard deviation $\sigma$ within each image were compared to the grayscale spectrum of the entire image. Based on this grayscale analysis of the entire image, thresholds were defined to differentiate CSH, portlandite and unhydrated particles, in accordance with methods proposed for the BSE image segmentation of cement pastes [9]. The threshold used to differentiate CSH from portlandite and portlandite from anhydrous particles will be referred to as $t_1$, resp. $t_2$ [11]. By comparing $m$ with $t_1$ and $t_2$, and $\sigma$ with $m$, the phase of each indent was thus inferred as CSH, portlandite, unhydrated particles or interface, e.g. an indent located close to two different phases, as based on Eq. (9). The final phase inference based on SEM images was visually verified. Some examples of inferences based on SEM images, with eventually triangular-shaped indents, are illustrated in Figure 3.

$$phase = \begin{cases} interface\ if\ \sigma > 0.35\ m \\ else: \begin{cases} CSH\ if\ m < t_1 \\ portlandite\ if\ t_1 < m < t_2 \\ unhydrated\ particle\ if\ m > t_2 \end{cases} \end{cases} \tag{9}$$

#### 2.3.3. Auto-NI-SEM coupling

In order to overcome the limitations of statistical data deconvolution and reduce variability of the identified phase properties, additional information has been brought by coupling nanoindentation data with BSE image analysis. For each indent, the natures of indents predicted by GMM deconvolution on the one hand, and SEM image analysis on the other hand, both methods were compared following the process described in Figure 4. Threshold values were identified by locating the minima in the grey value histogram, corresponding to the boundaries between distinct phases. The selection of these threshold values was then visually verified by overlaying the segmentation on the original SEM images to ensure robustness and accuracy. When the indents natures were predicted to be the same, the indent was then assigned to that of the predicted phase; otherwise, the indent was considered as

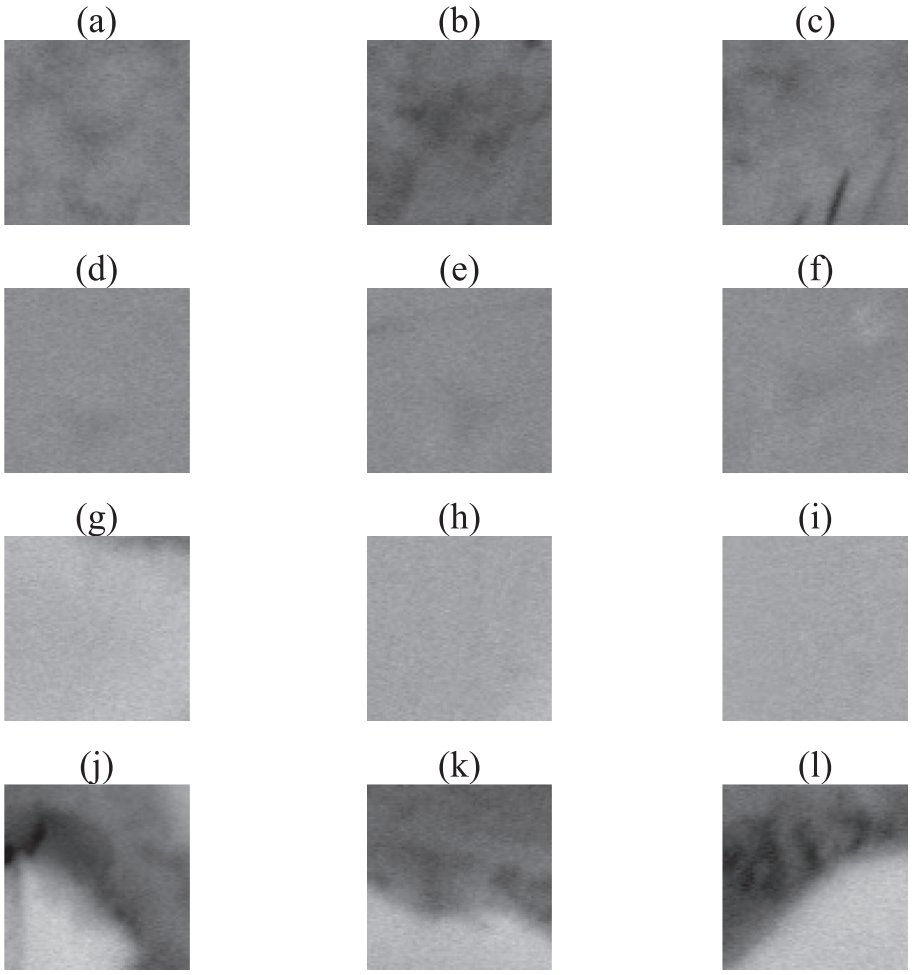


**Figure 3.** Example of phase inferences using SEM images of OPC-0.23: (a-c) CSH, (d-f) portlandite, (g-i) unhydrated particle and (j-l) interfaces. All the images dimensions are 2.67 μm.

unreliable information and not taken into account when recalculating/assessing the properties of a single phase. This approach reduces the likelihood of incorrectly assigning the indent to the wrong phase.

As explained above, the output of BSE image analysis is always composed of four groups (CSH, portlandite, interfaces, unhydrated cement particles), while the GMM classification depends on the mix and the clusters are assigned based on their mean values and standard deviation. Generally speaking, GMM cannot detect phases with small amounts as individual clusters; instead, they are intermixed in a cluster with another phase of higher quantity and similar properties. Such is the case for portlandite in cement pastes of a low water-to-cement ratio, which was also claimed by Wei *et al.* [54], whereby the cluster likely to contain two phases predicted by GMM and identified by its high standard deviation is then compared to both probable existing individual phases predicted by phase inference using SEM images (as will be detailed in the case described below in Section 3.1.3). This coupling method results in 24 % to 43 % non-corresponding phase inference depending on the mix.

## 3. Results and discussion

### *3.1. Micromechanical properties of the cement paste: GMM vs. Auto-NI-SEM coupling*

#### *3.1.1. GMM deconvolution results*

Using GMM clustering, three clusters were found in OPC-0.23, as depicted in Figure 5. Table 2 lists the elastic properties and volume fraction of each cluster. Based on these properties, clusters 1 and 3 were assigned to HD CSH and unhydrated cement particles, respectively. As for cluster 2, it can be noticed that the standard deviation of properties is high, which suggests that the indents do not belong to a pure single phase. According to the mean values, this cluster can be assigned to portlandite and some of the indents on interfaces between hydration products and unhydrated cement particles.

Figure 6 shows the whole SEM image of the indented area, along with the location of indents and their nature predicted by GMM clustering, and then the 1/4 of the image for a better visualization. It seems that the predictions given by GMM are quite good. Based on visual inspection by a microscopy specialist, the GMM predictions are found to be in good agreement with observations from SEM images. In the remainder of the manuscript, GMM deconvolution is treated as the benchmark method for evaluating the proposed methodology.

Indeed, most of the indents assigned to lie in cluster 1 (red squares) are indeed located in CSH, likewise for black squares of portlandite and indents on the interfaces. Blue squares, corresponding to cluster 3, are mainly located in unhydrated cement particles (light gray in the SEM image). Prior to numerical clustering, indents with high properties ($E > 220$ GPa or $H > 12$ GPa) were filtered given the finding of their negative impact on clustering (numerical clustering is sensitive to outliers). The image also indicates that the 7 filtered indents were located either in periclase, shown in the SEM image as dark spots in the unhydrated cement grains, or in $C_4AF$ (which appears lighter than other clinker phases due to the presence of Fe). This finding is consistent with results obtained using molecular dynamics-based simulations, whereby the

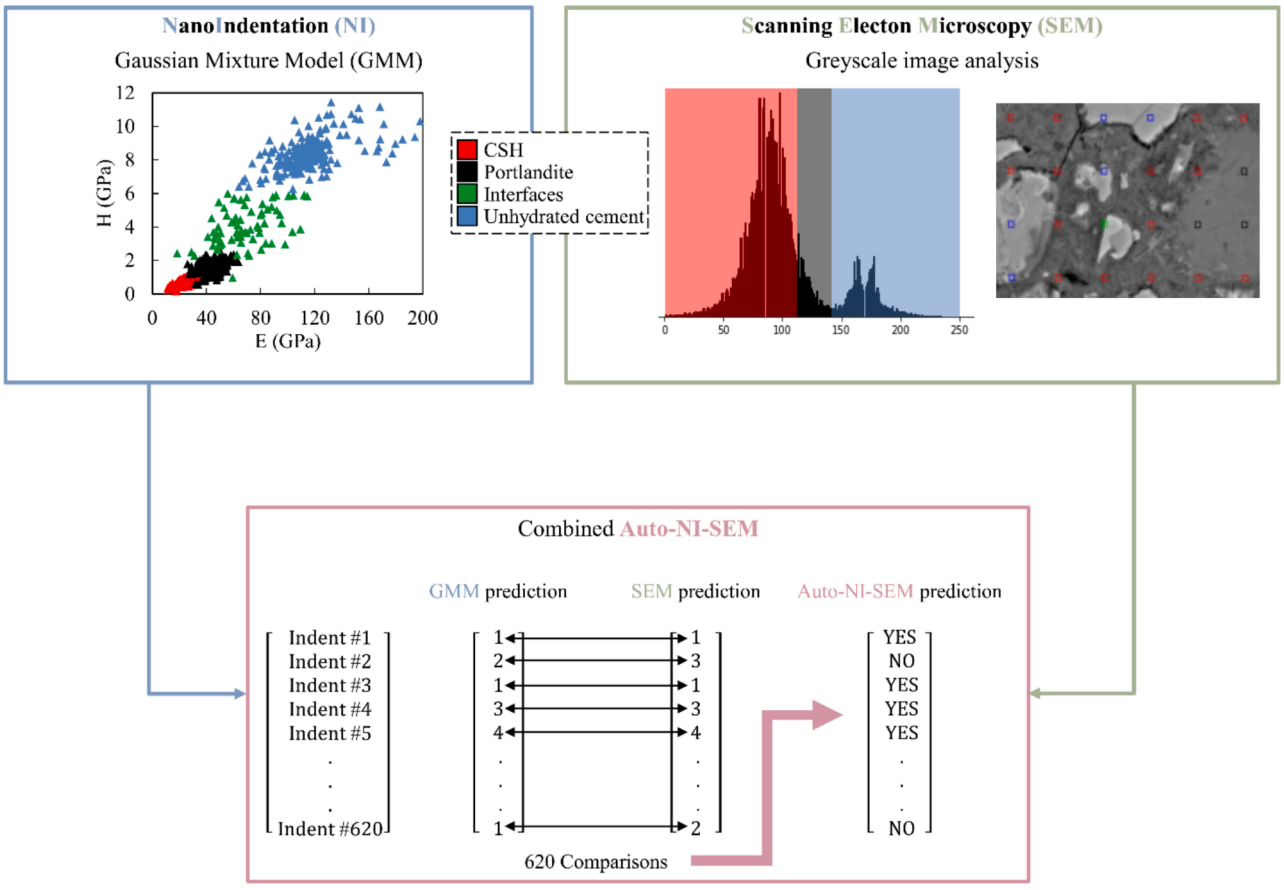


**Figure 4.** Flowchart for Auto-NI-SEM coupling method.

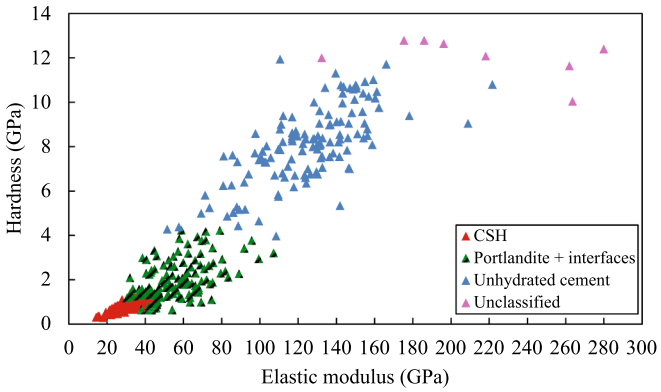


**Figure 5.** Scatterplot of OPC-0.23 micromechanical properties and cluster distribution obtained using GMM deconvolution.

**Table 2**
Statistical deconvolution results for OPC-0.23 (mean ± standard deviation).

| | Cluster 1 | Cluster 2 | Cluster 3 |
|---|---|---|---|
| E (GPa) | 30.2 ± 5.2 | 55.6 ± 15.1 | 125.4 ± 27.3 |
| H (GPa) | 0.81 ± 0.17 | 1.96 ± 0.86 | 8.08 ± 1.73 |
| fr[a] | 0.585 | 0.206 | 0.197 |
| Predominant phase | HD CSH | CH + interfaces | Unhydrated cement |

[a] A fraction of 0.012 was not classified.

elastic modulus of these phases was reported to be greater than 205 GPa [55]. Nevertheless, some indents on interfaces were numerically identified as portlandite (see examples circled in orange in Figure 6). Also, some indents circled in purple in Figure 6 lie in CSH yet had been identified as belonging to portlandite via GMM and portlandite identified as CSH (cyan circles). This observation proves the limitation of numerical clustering for indents of intermediate properties.

### 3.1.2. SEM-BSE analysis results

According to the method described in Section 2.3.3, the indents were classified into four groups: CSH, portlandite, unhydrated cement, and interfaces between hydration products and unhydrated clinker particles. The predicted natures are illustrated on the SEM image in Figure 7 on the same portion as in Figure 6, and the scatterplot of elastic properties in Figure 8. It can be noticed that the majority of indents located in unhydrated cement grains were correctly assigned since the grayscale values of these particles are well distinguished from the peak of hydrates. However, some cement particles containing periclase that appear as dark gray to black spots were incorrectly predicted as CSH due to their gray level belonging to hydration products peak. These indents appear in the scatterplot in Figure 8 as red points around the agglomeration of blue points (unhydrated cement cluster). Consequently, the properties of periclase can be precisely determined by averaging the properties of indents located in periclase on the SEM image. It was thus derived that E = 208.8 ± 53.9 GPa and H = 9.70 ± 1.29 GPa, both of which are consistent with [55], with a fraction of 0.039 of the total indents in unhydrated cement (once again consistent with the value given in the cement composition in Table 1).

Based on a visual observation of phases in Figure 7, it can be noticed that the nature of most indents located in hydration products and interfaces has been well predicted. On the other hand, plotting their micromechanical properties in Figure 8 reveals that the predicted natures may not all be correct. This outcome may be due to errors in the indent location, as induced from two main sources: one originating from

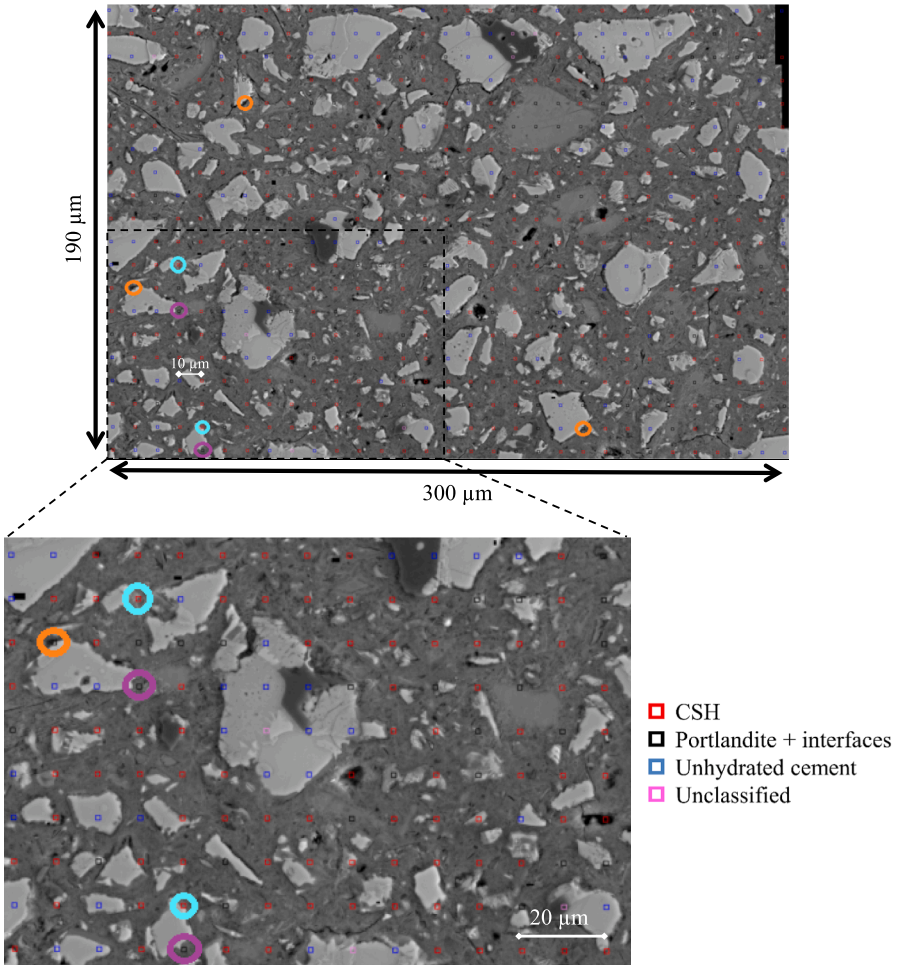


**Figure 6.** Representation on an OPC-0.23 SEM image of the nature of indents predicted by GMM deconvolution.

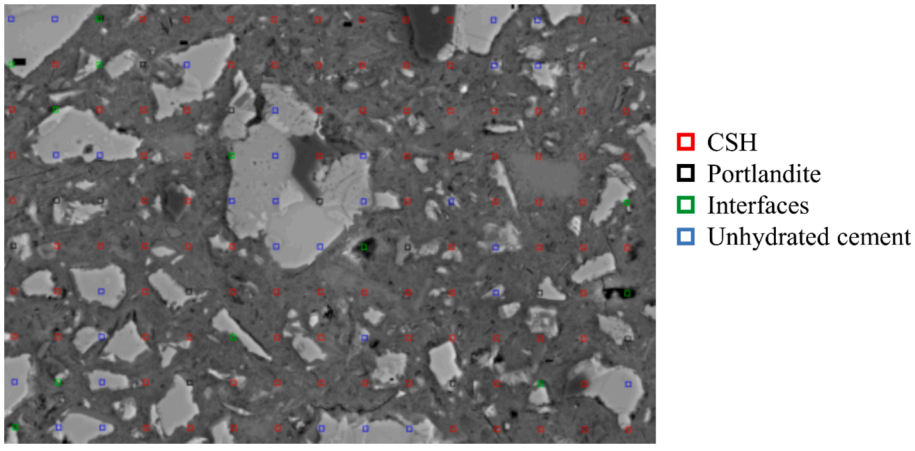


**Figure 7.** Representation on a portion of OPC-0.23 SEM image of the nature of indents predicted by grayscale SEM image analysis.

SEM image assemblage, the other corresponding to indenter movement errors (which account for roughly 6 % of the distance between two successive indents).

### 3.1.3. *Auto-NI-SEM coupling results*

Figure 9 displays the results of this coupling with the corresponding phase predictions, by means of both GMM and grayscale analysis deconvolution processes, as represented in the same colors as above on the same portion of the image, along with the unmatching indents in yellow boxes. These latter correspond to indents that were clustered into different phases by GMM and SEM image analysis. In checking the predicted natures in the corresponding indents, no false prediction was found. Moreover, the figure shows that of the 620 indents, 186 are noncorresponding indent natures, amounting to 30 % of the total number of indents. As presented in [56], the nanoindentation measurements are indeed heavily influenced by boundary conditions, and the interaction volume under the indenter is greater than the visible indent imprint, especially for elastic modulus measurement. Also, some

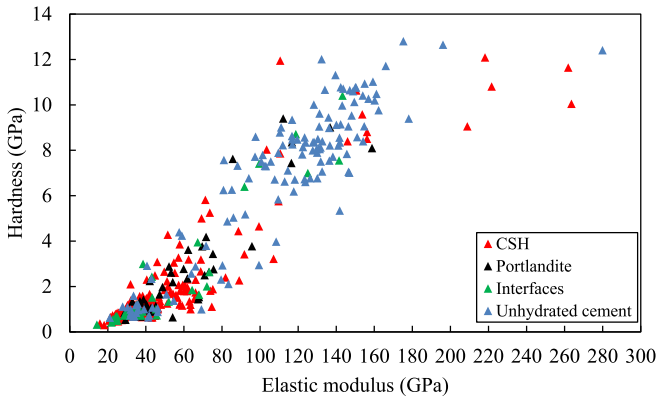


**Figure 8.** Scatterplot of OPC-0.23 micromechanical properties and cluster distribution obtained using SEM image analysis.

indents belonging to CSH have been incorrectly predicted due to the presence of some nanoporosity in black, which may be assessed as an interface according to grayscale analysis. For indents near the phase interfaces, their natures may be incorrectly predicted owing to the error on indent localization. Lastly, the few indents belonging to unhydrated cement particles (located either in periclase or on the edge between $C_4AF$ and the rest of a clinker particle) were incorrectly predicted using SEM as CSH and interfaces, respectively, hence incorrectly predicted by the coupling.

Figure 10 shows a more detailed visualization of the unmatching indents through histograms of micromechanical properties. These histograms reveal that the majority of noncorresponding indents belong to intermediate indents between clusters, with some lying in the cluster of unhydrated cement, as previously observed visually. Consequently, the distributions of pure single phases (CSH, portlandite and unhydrated cement) in elastic modulus, hardness and contact creep modulus do not overlap and are tighter, which is indeed the aim of this coupling method.

To highlight the benefits of the proposed method, a comparison of the mean and standard deviation of the micromechanical phase properties is shown in Figure 11. It can be noticed that the elastic modulus of the phases is mainly the same, but the error is reduced by nearly 5 % and 17.4 % resp. for CSH and unhydrated cement grains. Interestingly, this error reduction reaches 48.6 % for the contact creep modulus of CSH, which leads to a more accurate assessment of the creep behavior of materials. This error reduction in micromechanical properties is also observed for the other cement pastes with different water-to-cement ratios (these results will be presented further below).

A second benefit of this method pertains to the determination of portlandite amount in the mix, especially when this amount is relatively minor, e.g. in the case of a cement paste with a water-to-cement ratio of 0.23. Numerical clustering cannot distinguish these few points of intermediate mechanical properties as an individual cluster. Hence, the indents belonging to portlandite are generally predicted to lie in a cluster where they are intermixed with another phase featuring similar properties, which is the case here in cluster 2, where they are intermixed with indents on interfaces between hydrates and unhydrated cement. Figure 12 indicates the volumetric content of portlandite in OPC-0.23, as determined by GMM, SEM imaging, the combined method and TGA for purposes of comparison. Among the four different techniques, the value determined by TGA might be considered as reference for the determination of portlandite content. Relative to this measurement, BSE image analysis predicted the portlandite content with an error of 3.8 %, thus confirming the good accuracy of this method. Conversely, numerical clustering cannot detect portlandite as a separate cluster and indicates a total content of 20.6 % for both interfaces and portlandite, while the combined method estimates portlandite content with a 29 % error with respect to the TGA result. Given the histograms of mechanical properties presented in Figure 10, it can be observed that some portlandite indents probably assumed to belong to cluster 2, but predicted as Cluster 1 using GMM, were excluded by the combined method. Consequently, the portlandite content correctly determined by BSE image analysis was reduced when combined with GMM. Nonetheless, the combined method can still be useful in generating a qualitative idea of the actual portlandite content in cement pastes with a lower portlandite content.

It can be deduced that introduction of Auto-NI-SEM method enables the definition of an individual cluster for portlandite while the water-to-cement-ratio of the paste is low, with an acceptable error on the calculated volume fraction, which was not possible using only statistical deconvolution.

### *3.2. Application of the coupling to phase quantification and the impact of mix design parameters on CSH micromechanical properties*

#### *3.2.1. Phase quantification assessed by Auto-NI-SEM*

While the methodology is initially demonstrated on an OPC-0.23 paste in Section 3.1, the same approach, illustrated in Figure 13, was systematically applied to three additional cement pastes with varying water-to-cement (w/c) ratios.(0.3, 0.35 and 0.4). This broader validation, combined with comparisons to data from the literature and reliable experimental measurements, is intended to underscore the robustness and generalizability of the proposed method for diverse hydration product compositions and w/c ratios. The proportions of major phases obtained using the Auto-NI-SEM method are shown in Figure 14. These volume fractions were calculated after removal of indents belonging to interfacesas illustrated in Figure 5 and 6. It can be noticed that in relatively low water-to-cement ratio cement pastes, HD CSH is the

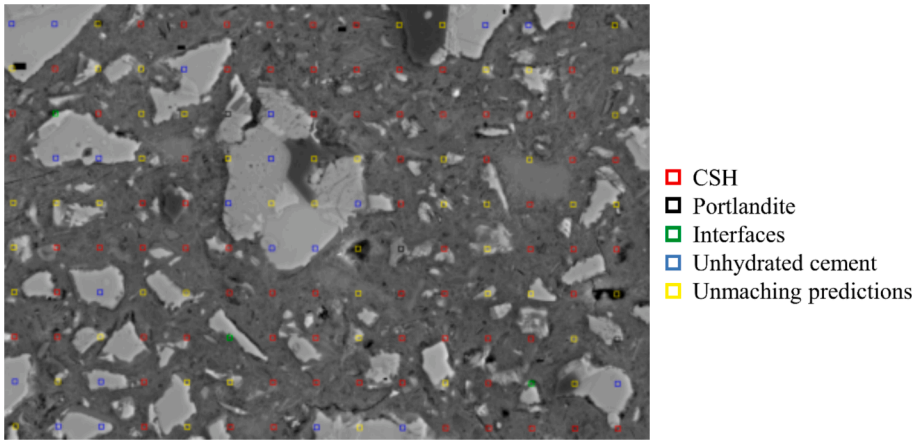


**Figure 9.** Representation on a portion of OPC-0.23 SEM image of indent nature as predicted by Auto-NI-SEM.

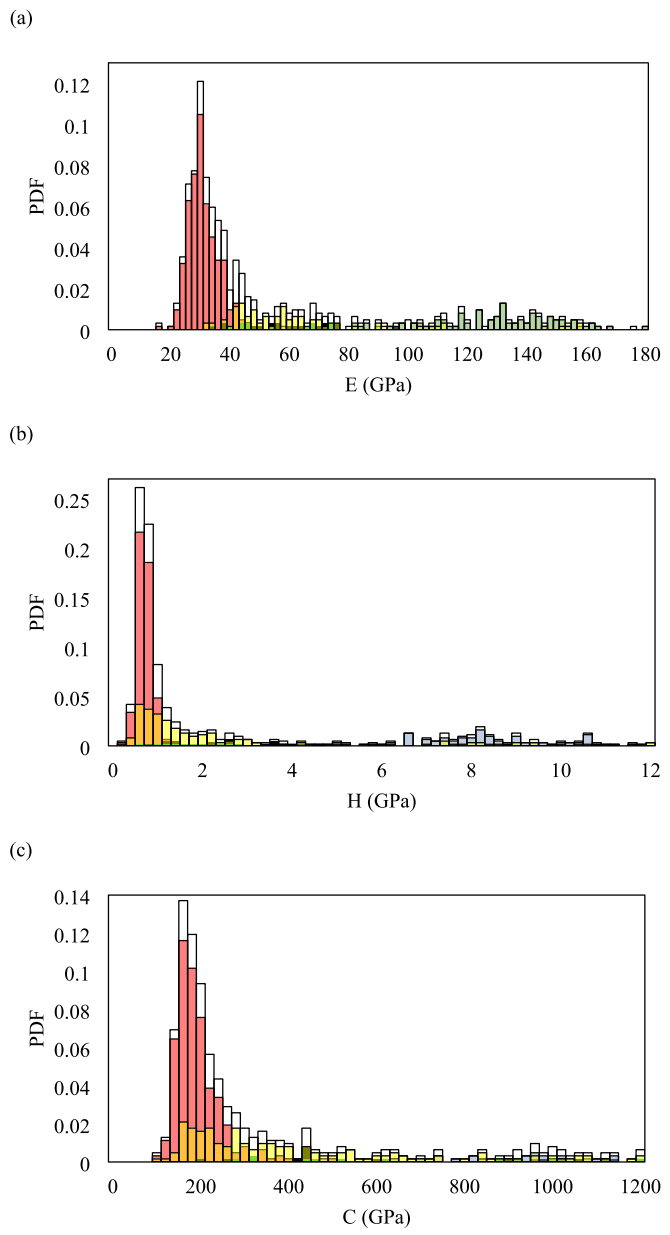


**Figure 10.** Histograms of distributions of the indentation output variables of OPC-0.23 after coupled GMM and SEM image analysis clustering: (a) Young's modulus, (b) hardness and (c) contact creep modulus. The total distribution is depicted by the continuous black line in white, while the phase distributions are colored in red (CSH), black (portlandite), green (interfaces) and blue (unhydrated cement). The distribution of noncorresponding indents is shown in yellow. The colors are transparent.

predominant form of CSH in the mix. However, when the water-to-cement ratio is increased to 0.4, a cluster of LD CSH appears and is predominant relative to HD CSH. It can also be noticed that the higher the water-to-cement ratio, the higher is the amount of both CSH and portlandite as the main hydration products of Portland cement pastes and the lower the proportion of the remaining unhydrated cement grains. Compared to the volume fractions calculated on several SEM images by Wong and Buenfeld [9], those determined by nano-indentation are very close to one another. The volume fractions assessed using this method can in fact directly serve as input data in homogenization schemes, rather than those stemming from other time-consuming experimental methods, as widely practiced nowadays.

Figure 15 shows the portlandite content of the cement pastes

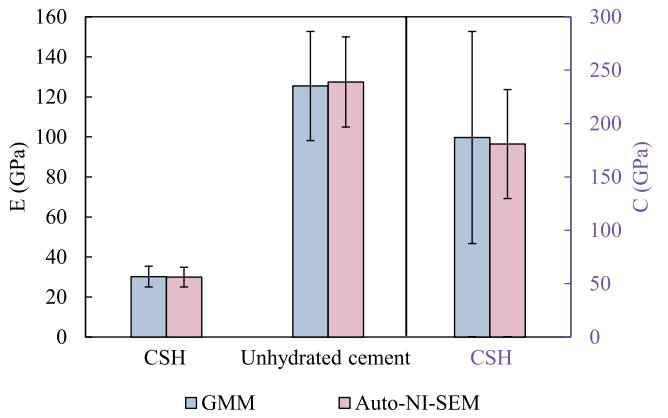


**Figure 11.** Micromechanical property refinement of OPC-0.23 by means of Auto-NI-SEM coupling.

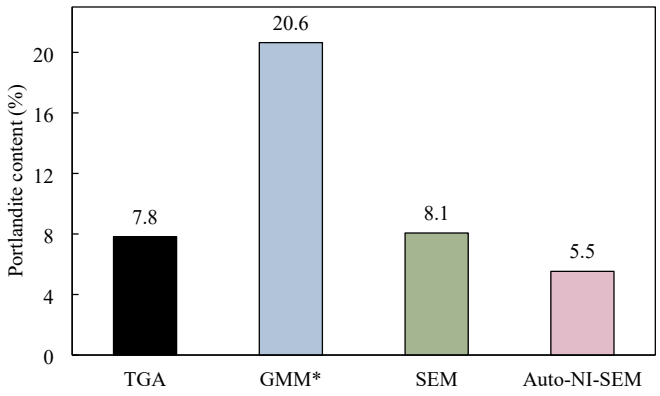


**Figure 12.** Portlandite content in OPC-0.23 using various deconvolution methods. *The portlandite cluster is also likely to contain interfaces.

assessed by the three deconvolution methods (i.e. GMM, BSE image analysis, the coupled method) versus the portlandite content determined by TGA results. In low water-to-cement ratio cement pastes (0.23 and 0.3), portlandite content is low; therefore, the phase could not be numerically detected as an individual cluster using GMM but instead intermixed with phases whose properties may be similar, i.e. some particles of HD or UHD CSH and interfaces between hydration products and unhydrated cement. However, the combined Auto-NI-SEM method could construct a cluster with this individual phase, yielding relatively underestimated volume fractions with respect to the linear fitting $P_{Auto\text{-}NI\text{-}SEM} = 0.7231\ P_{TGA}$, though well correlated with what was calculated by TGA ($R^2 = 0.83$). This underestimation is due to false portlandite inference by GMM (as shown above in Figure 6), which degrades the correspondence of some SEM-predicted portlandite indents. Interestingly, fitting a linear relation to the BSE-SEM image deconvolution method with TGA results yielded $P_{SEM} = 0.9941\ P_{TGA}$, with an average distance of the obtained points to the fitted line equal to 0.2 %. The amount of portlandite predicted by this method perfectly matches the values obtained by TGA, thus confirming its effectiveness in determining portlandite content in various cement pastes, including those with low water-to-cement ratios. For cement pastes with water-to-cement ratios of 0.35 and 0.4, the amount of portlandite measured using GMM was relatively good. We can thus conclude that GMM can be trusted whenever the actual amount of the phases is greater than or equal to 12.8 % or else lie between 10.7 % and 12.8 % (i.e. the portlandite amounts determined by the TGA of cement pastes, where GMM might or might not detect an individual cluster for portlandite).

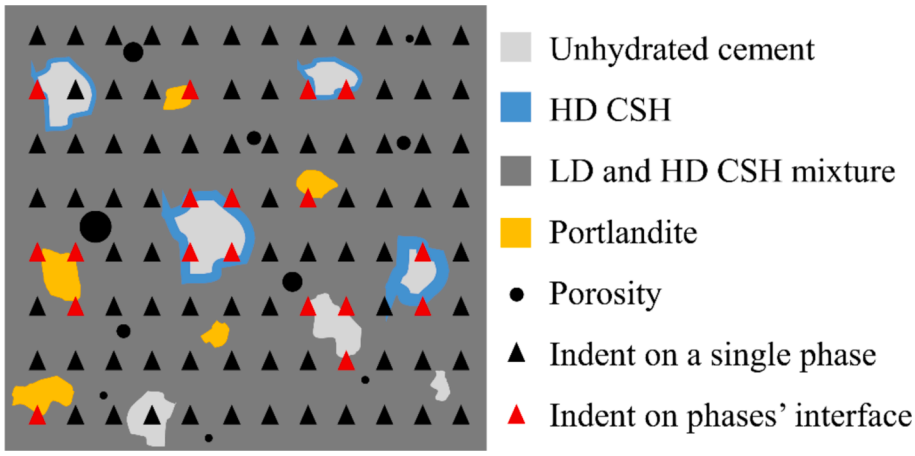


**Figure 13.** Schematic representation of indents on interfaces deleted by Auto-NI-SEM coupling method (red indents).

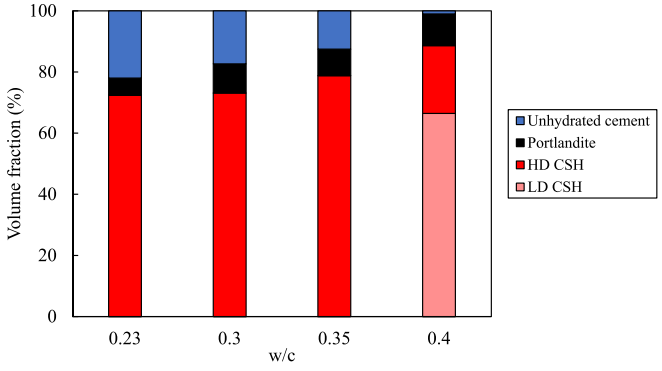


**Figure 14.** Cement paste compositions according to the Auto-NI-SEM coupling deconvolution method.

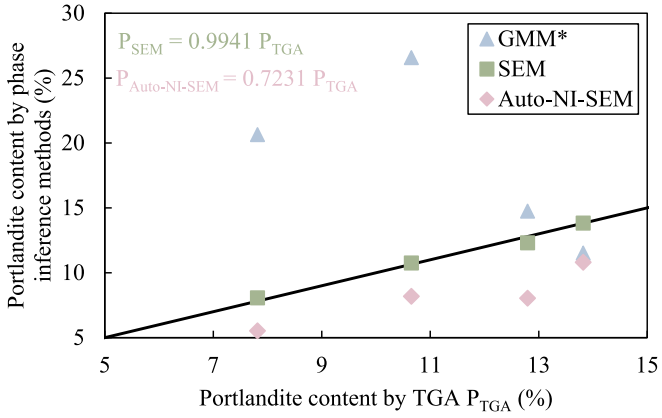


**Figure 15.** Portlandite content in the cement pastes using various methods. *The portlandite cluster is also likely to contain interfaces.

### 3.2.2. The effect of water-to-cement ratio and gel porosity on CSH micromechanical properties

Using the combined Auto-NI-SEM deconvolution method described above, the CSH Young's modulus and contact creep modulus were calculated; directly for the pastes with w/c up to 0.35, and using Mori-Tanaka homogenization scheme for OPC-0.4, as two different types of CSH were detected by deconvolution (LD CSH was considered as the matrix with inclusions of HD CSH given their relative volume proportions). Then, their evolution with respect to water-to-cement ratio and gel porosity accessible to MIP measurements is shown in Figure 16. Gel porosity was taken as the fraction of pores with a diameter smaller than 10 nm, as based on MIP measurements.

Figure 16 shows that both CSH properties decrease with water-to-cement ratio and gel porosity accessible to MIP. The elastic modulus seem to linearly decrease with water-to-cement ratio with a good correlation ($R^2 = 0.97$), as well as with the amount of gel porosity accessible to MIP in the paste ($R^2 = 0.96$). As for the contact creep modulus, we can notice that it is more correlated with gel porosity accessible to MIP ($R^2 = 0.75$) than with w/c ratio ($R^2 = 0.65$), yet remains less well correlated to mix design properties than the elastic modulus. Up to w/c = 0.35, the contact creep modulus values in the three cement pastes do not vary much, especially given the overlapping error bars even with reduced uncertainties, lying in the range of [165 GPa, 190 GPa], which is consistent with the values reported in [37,57]. For w/c = 0.4, C drops to 149.9 GPa, which can be explained by the predominance of LD CSH in the total amount of CSH in this paste, as detected by statistical deconvolution (*C* is calculated for LD CSH and HD CSH separately as 128.5 ± 40.5 GPa and 235.8 ± 80.3 GPa, respectively). This decreasing trend of the CSH micromechanical properties is in accordance with [58]: as the water-to-cement ratio increases, porosity increases and more space becomes available for hydration products to be precipitated, namely for CSH. Consequently, the formation of CSH gel with lower packing densities, likely to exhibit poorer mechanical and viscoelastic properties is promoted, and the amount of LD CSH in the total CSH content is higher. Thanks to the coupling method, a very good correlation is found between CSH Young's modulus and gel porosity accessible to MIP.

## 3.3. Application of the coupling to viscoelastic properties homogenization

### 3.3.1. Process

In this section, we propose to demonstrate the benefits of the refinement of viscoelastic properties and the quantification of phases provided by the Auto-NI-SEM coupling method, compared to GMM statistical deconvolution, in the prediction of cement paste creep.

For this purpose, an analytical viscoelastic homogenization model is used, supplied by output data from GMM deconvolution on the one hand, and from the coupled Auto-NI-SEM method on the other; the homogenized creep moduli will subsequently be compared with the experimental paste creep modulus measurement, carried out via microindentation. The porosity was taken into account in the homogenization model in form of capillary porosity, with diameters ranging from 10 nm to 10 μm. Indeed, pores with diameters below this range are already included in the nanoindentation measurement, and those with higher diameters are too large for the surface of influence induced by a microindentation measurement (~50 μm). In addition to the capillary porosity, the viscoelastic homogenization model uses as input data the

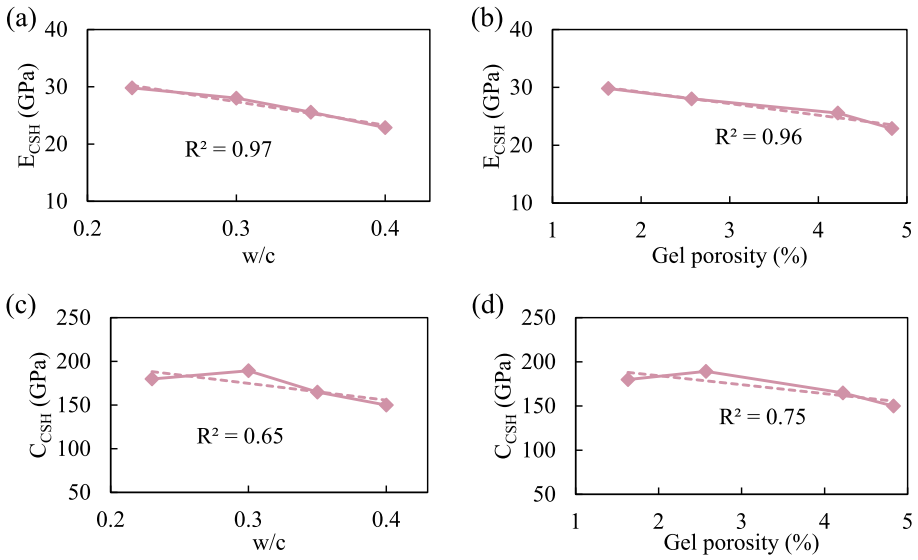


**Figure 16.** Evolution of mechanical and viscoelastic properties of CSH, as obtained using the coupled Auto-NI-SEM technique with water-to-cement ratio and gel porosity accessible to MIP: (a) $E_{CSH}$ = f(w/c), (b) $E_{CSH}$ = f(gel porosity), (c) $C_{CSH}$ = f(w/c), (d) $C_{CSH}$ = f(gel porosity).

respective contact creep moduli of the different cementitious phases, as well as their volume fractions normalized taking capillary porosity into account; these parameters are provided by the two deconvolution methods, GMM and Auto-NI-SEM. The approach thus described is illustrated in Figure 17.

### 3.3.2. *Analytical model for viscoelastic homogenization*

Concrete is a composite material containing several phases; these phases can be divided on several scales, as suggested by Bernard *et al.* [59]. Up to the paste scale, which falls within the scope of our study, two levels can be distinguished: one at the CSH matrix scale and a second at the paste scale, as illustrated by the diagram in Figure 18. The analytical model described below has been proposed and validated in several studies [38,36,37].

At the first level, the two phases involved are low and high density CSH, which can be viewed as elliptical inclusions embedded in a matrix, depending on their relative volume fractions (the one with the higher volume fraction is considered as matrix, and the other as inclusion), in the Mori-Tanaka (MT) scheme. The Laplace-Carson transformation of the volumetric and deviatoric components of creep compliance, respectively $J^{vol}$ and $J^{dev}$, can be written as follows:

$$J^{vol}_{MT} = \frac{f_m + f_i\left[1+\alpha\left(\frac{J^{vol}_m}{J^{vol}_i}-1\right)\right]^{-1}}{\frac{f_m}{J^{vol}_m} + \frac{f_i}{J^{vol}_i}\left[1+\alpha\left(\frac{J^{vol}_m}{J^{vol}_i}-1\right)\right]^{-1}} \tag{10}$$

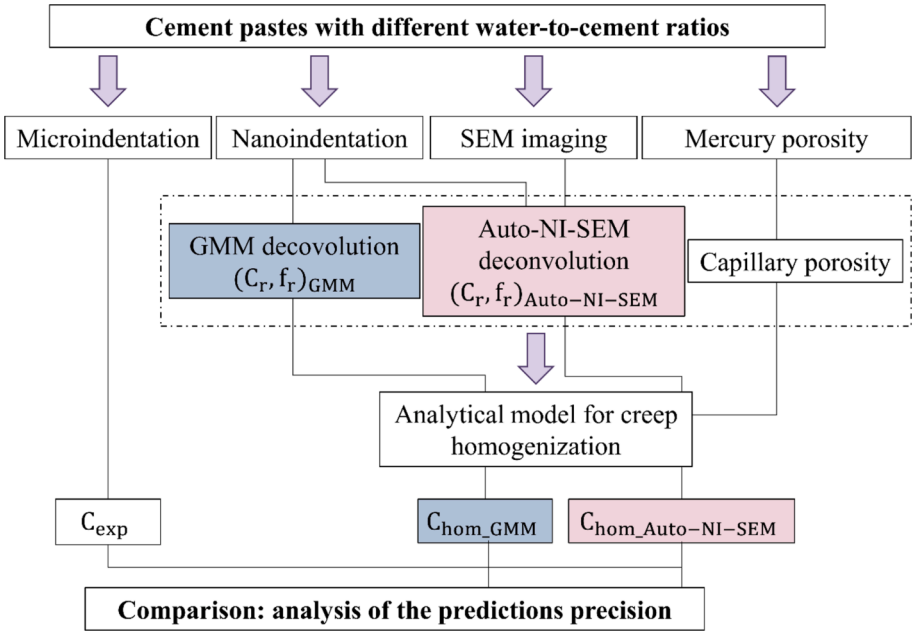


**Figure 17.** Diagram of the homogenization process for precision analysis of input data.

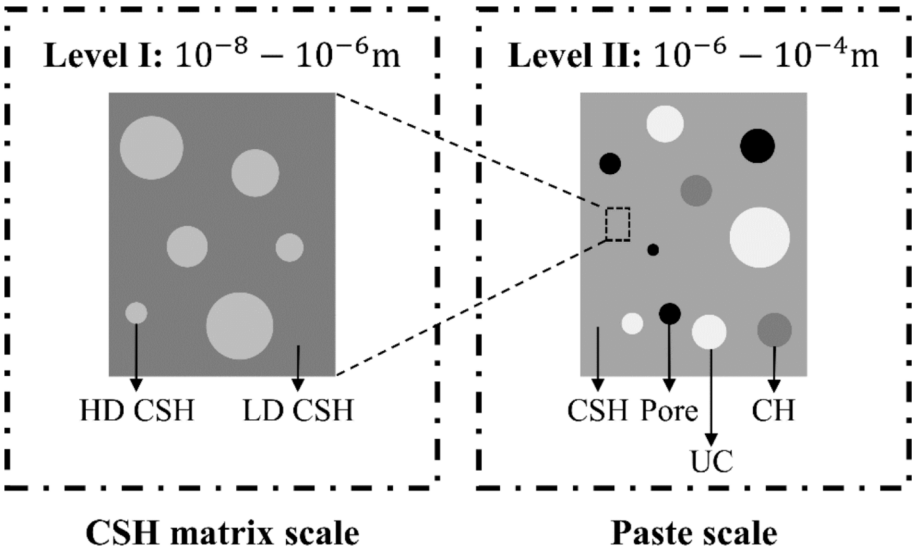


**Figure 18.** Modeling the multiscale microstructure of the cement pastes, adapted from [9].

$$J_{MT}^{dev} = \frac{f_m + f_i[1+\beta\left(\frac{J_m^{dev}}{J_i^{dev}} - 1\right)]^{-1}}{\frac{f_m}{J_m^{dev}} + \frac{f_i}{J_i^{dev}}[1+\beta\left(\frac{J_m^{dev}}{J_i^{dev}} - 1\right)]^{-1}} \tag{11}$$

where $\alpha = 3J_m^{dev}/(3J_m^{dev}+4J_m^{vol}), \beta = 6(J_m^{dev}+2J_m^{vol})/5(3J_m^{dev}+4J_m^{vol})$, $f$ is the volume fraction, $i$ and $m$ denote inclusion and matrix respectively.

Based on the logarithmic creep of cementitious materials, the complacency components can be written as $J_x^y = -\ln(p)/C_x^y$; $x \in \{i, m\}$ *and* $y \in \{vol, dev\}$. Substituting in equations (10) and (13) we obtain the Laplace transformations of the contact creep modulus of CSH, volumetric $C^{vol}$ and deviatoric $C^{dev}$:

$$C_{CSH}^{vol} = \frac{f_m C_m^{vol} + f_i C_i^{vol}[1+\alpha\left(\frac{C_i^{vol}}{C_m^{vol}} - 1\right)]^{-1}}{f_m + f_i[1+\alpha\left(\frac{C_i^{vol}}{C_m^{vol}} - 1\right)]^{-1}} \tag{12}$$

$$C_{CSH}^{dev} = \frac{f_m C_m^{dev} + f_i C_i^{dev}[1+\beta\left(\frac{C_i^{dev}}{C_m^{dev}} - 1\right)]^{-1}}{f_m + f_i[1+\beta\left(\frac{C_i^{dev}}{C_m^{dev}} - 1\right)]^{-1}} \tag{13}$$

where $\alpha = 3C_m^{vol}/(3C_m^{vol}+4C_m^{dev})$, $\beta = 6(C_m^{vol}+2C_m^{dev})/5(3C_m^{vol}+4C_m^{dev})$. On the other hand, and with regard to the elasticity of materials, the relationship between the indentation modulus $E$, the bulk modulus $K$ and the shear modulus $G$ can be expressed as follows:

$$E = 4G\frac{3K+G}{3K+4G} \tag{14}$$

The Laplace transformation applied to equation (14) links the volumetric and deviatoric components of the CSH contact creep modulus, $C_{CSH}^{vol}$ and $C_{CSH}^{dev}$ respectively, to the homogenized CSH contact creep modulus $C_{CSH}$ by the equation:

$$C_{CSH} = 4C_{CSH}^{dev}\frac{3C_{CSH}^{vol} + C_{CSH}^{dev}}{3C_{CSH}^{vol} + 4C_{CSH}^{dev}} \tag{15}$$

Assuming that the nanoindentation test has a negligible effect on the density of CSH (or any other cementitious phase), we can write that: $C_{CSH}^{vol} \approx +\infty$, and thus equation (15) implies that $C_{CSH} = 4C_{CSH}^{dev}$, $C_m^{dev} = C_m/4$, $C_i^{dev} = C_i/4$ and $\beta = 2/5$ ($C_i$ and $C_m$ being the contact creep moduli of low and high density CSH, depending on their relative volume fractions, measured directly by nanoindentation). Finally, we obtain:

$$C_{CSH} = \frac{f_m C_m + f_i C_i[1+\frac{2}{5}\left(\frac{C_i}{C_m} - 1\right)]^{-1}}{f_m + f_i[1+\frac{2}{5}\left(\frac{C_i}{C_m} - 1\right)]^{-1}} \tag{16}$$

In our case, homogenization at this level only concerns OPC-0.4 paste, since deconvolution allows us to distinguish between two types of CSH. On the other hand, and given that the volumetric fraction of low-density CSH is greater than that of high-density CSH (see Figure 17); the latter are therefore considered as inclusions and low-density CSH as matrix in the Mori-Tanaka model in the contact creep modulus of CSH calculation.

At the second level of cement paste, the phases of CSH, portlandite, unhydrated cement and porosity are taken into account. Assuming that $C_{pore} = 0$ GPa, and that the distribution of the other three phases is disordered, the self-consistent (SC) scheme is used for homogenization at this scale. For this purpose, the formulas for the volumetric and deviatoric components of creep compliance are given by the Laplace-Carson transformation as follows:

$$J_{SC}^{vol} = \frac{\sum_r f_r[1+\alpha\left(\frac{J_{SC}^{vol}}{J_r^{vol}} - 1\right)]^{-1}}{\sum_r \frac{f_r}{J_r^{vol}}[1+\alpha\left(\frac{J_{SC}^{vol}}{J_r^{vol}} - 1\right)]^{-1}} \tag{17}$$

$$J_{SC}^{dev} = \frac{\sum_r f_r[1+\beta\left(\frac{J_{SC}^{dev}}{J_r^{dev}} - 1\right)]^{-1}}{\sum_r \frac{f_r}{J_r^{dev}}[1+\beta\left(\frac{J_{SC}^{dev}}{J_r^{dev}} - 1\right)]^{-1}} \tag{18}$$

where $r$ describes the different phases taken into account at this scale, $\alpha = 3J_{SC}^{dev}/(3J_{SC}^{dev}+4J_{SC}^{vol}), \beta = 6(J_{SC}^{dev}+2J_{SC}^{vol})/5(3J_{SC}^{dev}+4J_{SC}^{vol})$.

Using the same development described above, the creep modulus of the cementitious paste $C_{paste}$ can be calculated as follows:

$$C_{paste} = \frac{\sum_r f_r C_r [1 + \frac{2}{5}\left(\frac{C_r}{C_{paste}} - 1\right)]^{-1}}{\sum_r f_r [1 + \frac{2}{5}\left(\frac{C_r}{C_{paste}} - 1\right)]^{-1}} \quad (19)$$

### 3.3.3. Results and discussion

Table 3 shows the homogenized creep modulus of the four pastes, using input data from GMM deconvolution ($C_{hom\_GMM}$) on the one hand, and from the Auto-NI-SEM coupled method ($C_{hom\_Auto\text{-}NI\text{-}SEM}$) on the other; the error of the homogenized creep modulus compared to the direct experimental measurement by microindentation was also evaluated.

From this table, we can see that this error is limited to 16 % using input data from both methods, validating the model's compatibility with the proposed problem and the assumptions taken into account in the calculation. This error varies between 0.6 % and 16 % using data from GMM deconvolution and between 0.9 % and 12 % using data from the coupled Auto-NI-SEM method. Comparing the two methods, we can notice that by supplying the model with the Auto-NI-SEM coupling results, the error on the homogenized creep modulus is generally lower, and that this method is more accurate on pastes with low w/c ratios. Using the data provided by the coupled method, we can see that the largest error is 12 % observed for paste OPC-0.35; this can be explained by the fact that the number of corresponding indents between GMM and SEM image analysis was the smallest among all the pastes. Looking at the Figure 19, and taking into account the standard deviation of the creep modulus of the pastes, measured by microindentation, we can see that all the homogenized creep modulus values $C_{hom\_Auto\text{-}NI\text{-}SEM}$ fall within these standard deviations, which is not the case for all the $C_{hom\_GMM}$ values, which are outside the standard deviation for OPC-0.23 and OPC-0.35.

Figure 19 also shows the evolution of the experimental and homogenized creep moduli of the four pastes with the water-to-cement ratio. It can be observed that the creep modulus of the cementitious pastes decreases with the w/c ratio, and that the general trend remains the same for homogenized creep moduli too. This trend was observed by Liang and Wei [60] on cement paste creep moduli calculated by microindentation, and by Le Roy on the same material but using macroscopic uniaxial creep tests [61].

Figure 20 shows the correlation between the creep moduli measured experimentally by microindentation of the different pastes, and those obtained by homogenization, of the data from GMM deconvolution on the one hand, and those from the Auto-NI-SEM coupling method on the other. This figure shows that the creep moduli obtained by the homogenization model supplied by both methods are linearly well correlated with those measured by microindentation. This linearity is expressed by the equation $C_{hom\_GMM} = 1.03\ C_{exp}$ for data obtained from GMM deconvolution, with an average error from experimental creep moduli of 20.9 GPa and a correlation coefficient $R^2 = 0.84$. As for the creep modulus correlation obtained using the coupling data, we find a linear relationship expressed by the equation $C_{hom\_Auto\text{-}NI\text{-}SEM} = 0.97\ C_{exp}$ but with a better correlation coefficient $R^2 = 0.94$ and a lower average error of 11.3 GPa; this proves the interest of the proposed coupling method for macroscopic creep prediction.

**Table 3**
Homogenized creep modulus (in GPa) of the different cement pastes and the error with respect to the creep modulus measured by microindentation.

| Paste reference | $C_{exp}$ | $C_{hom\_GMM}$ | Error | $C_{hom\_Auto\text{-}NI\text{-}SEM}$ | Error |
|---|---|---|---|---|---|
| OPC-0.23 | 260.1 | 296.5 | 14.0 % | 263.3 | 1.2 % |
| OPC-0.3 | 256.0 | 267.6 | 4.5 % | 258.5 | 0.9 % |
| OPC-0.35 | 213.5 | 178.7 | 16.3 % | 187.4 | 12.2 % |
| OPC-0.4 | 143.6 | 144.4 | 0.6 % | 130.0 | 9.5 % |

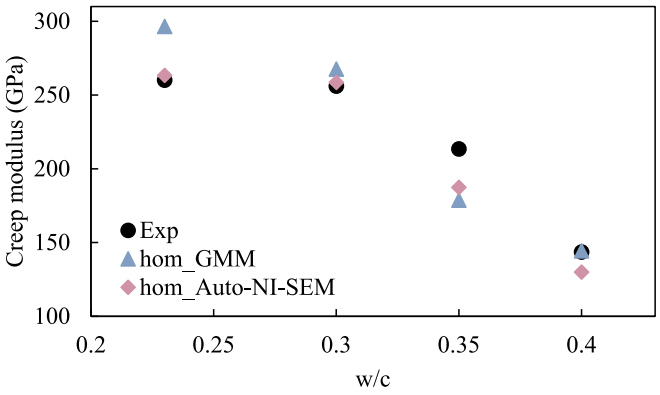


**Figure 19.** Creep modulus of the four cement pastes, experimental and homogenized, as a function of the water-to-cement ratio.

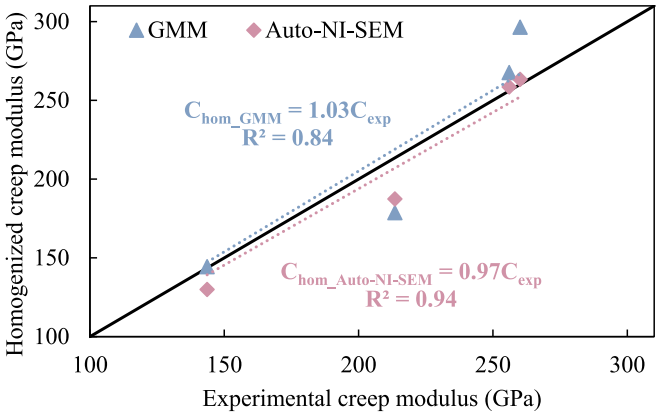


**Figure 20.** Homogenized creep modulus of the four cement pastes using input data from the two deconvolution methods, GMM and Auto-NI-SEM coupling, as a function of the creep modulus measured by microindentation.

## 4. Conclusion and perspectives

This study aimed to propose and validate a streamlined approach for processing nanoindentation data, integrating numerical and experimental deconvolution techniques. By coupling Gaussian Mixture Model (GMM) outputs with SEM-BSE grayscale image analysis, we developed a semi-automatic method to determine the micromechanical properties and volume fractions of major cement paste phases. The application of this method allowed effective re-establishment of some known effects of water-to-cement ratio variation on the properties of cement pastes.

The main findings can be summarized as follows:

- Sole reliance on SEM-BSE grayscale analysis risks inaccuracies due to surface-focused assessment and gray-level ambiguities. Nevertheless, it provided reliable quantification of portlandite content, as confirmed by thermogravimetric analysis.
- The proposed method Auto-NI-SEM reduced uncertainties in the derived micromechanical properties (elastic modulus by 5–18 % and viscoelastic properties by up to 48 %) and accurately assessed cement paste composition, including minor phases.
- Unlike GMM, the Auto-NI-SEM method successfully identified portlandite and periclase as distinct phases, even in challenging conditions such as low water-to-cement ratios, with results closely aligned with thermogravimetry.
- The strong correlation found between CSH's Young's modulus and separately water-to-cement ratio and gel porosity accessible to MIP confirms the validity of the proposed approach. This correlation was less strong for the CSH's contact creep modulus.

- Auto-NI-SEM-informed homogenization model enabled more accurate creep modulus predictions than GMM-informed one with respect to microindentation experimental measurements.

The proposed method has several inherent limitations that should be acknowledged. First, although the coupling eliminates some of GMM's wrong inferences, it relies on the results from the GMM, which means that any errors associated with the GMM may propagate into the proposed analysis. Second, the spatial resolution of phase segmentation is constrained by the spacing of the nanoindentation testing points, which may limit the method's ability to capture fine-scale phase variations. Finally, nanoindentation results are influenced by the phases beneath the surface, which cannot be detected through BSE imaging.

This work demonstrates the potential of the Auto-NI-SEM deconvolution method for micromechanical property characterization and composition analysis in cement pastes. Future applications would be to extend this approach to more complex systems, including those with mineral additions, to refine the detection of hydration products and predict the mechanical behavior of low-carbon binders. It would also be valuable to test the method on other heterogeneous materials at different scales.

## CRediT authorship contribution statement

**Imane Bekrine:** Writing – original draft, Visualization, Software, Investigation, Formal analysis, Data curation. **Benoit Hilloulin:** Writing – review & editing, Visualization, Validation, Supervision, Software, Methodology, Data curation, Conceptualization. **Ahmed Loukili:** Writing – review & editing, Supervision, Resources, Project administration, Funding acquisition.

## Declaration of competing interest

The authors declare that they have no known competing financial interests or personal relationships that could have appeared to influence the work reported in this paper.

## Data availability

The data that has been used is confidential.

## References


[1] K.L. Scrivener, R.J. Kirkpatrick, Innovation in use and research on cementitious material, Cem. Concr. Res. 38 (2008) 128–136, https://doi.org/10.1016/j.cemconres.2007.09.025.

[2] H.A. M, An Examination of Some Pore and Composite Portland Cement Pastes Using Scanning Electron Microscopy with X-ray Analytical Capability, Proceedings of the 8th International Congress on the Chemistry of Cement, 1986 4 (1986) 170–175.

[3] I.G. Richardson, The nature of C-S-H in hardened cements, Cem. Concr. Res. 29 (1999) 1131–1147, https://doi.org/10.1016/S0008-8846(99)00168-4.

[4] M. Vandamme, The nanogranular origin of concrete creep: a nanoindentation investigation of microstructure and fundamental properties of calcium-silicate-hydrates, L'ecole Nationale Des Ponts et Chaussées (2008).

[5] P. Stutzman, Scanning electron microscopy imaging of hydraulic cement microstructure, Cem. Concr. Compos. 26 (2004) 957–966, https://doi.org/10.1016/j.cemconcomp.2004.02.043.

[6] J. Bisschop, J.G.M. van Mier, How to study drying shrinkage microcracking in cement-based materials using optical and scanning electron microscopy? Cem. Concr. Res. 32 (2002) 279–287, https://doi.org/10.1016/S0008-8846(01)00671-8.

[7] X. Feng, E.J. Garboczi, D.P. Bentz, P.E. Stutzman, T.O. Mason, Estimation of the degree of hydration of blended cement pastes by a scanning electron microscope point-counting procedure, Cem. Concr. Res. 34 (2004) 1787–1793, https://doi.org/10.1016/j.cemconres.2004.01.014.

[8] S. Sahu, S. Badger, N. Thaulow, R.J. Lee, Determination of water–cement ratio of hardened concrete by scanning electron microscopy, Cem. Concr. Compos. 26 (2004) 987–992, https://doi.org/10.1016/j.cemconcomp.2004.02.032.

[9] H.S. Wong, N.R. Buenfeld, Determining the water–cement ratio, cement content, water content and degree of hydration of hardened cement paste: Method development and validation on paste samples, Cem. Concr. Res. 39 (2009) 957–965, https://doi.org/10.1016/j.cemconres.2009.06.013.

[10] B. Gaël, T. Christelle, E. Gilles, G. Sandrine, S.-F. Tristan, Determination of the proportion of anhydrous cement using SEM image analysis, Constr. Build. Mater. 126 (2016) 157–164, https://doi.org/10.1016/j.conbuildmat.2016.09.037.

[11] R.S. Edwin, M. Mushthofa, E. Gruyaert, N. De Belie, Quantitative analysis on porosity of reactive powder concrete based on automated analysis of back-scattered-electron images, Cem. Concr. Compos. 96 (2019) 1–10, https://doi.org/10.1016/j.cemconcomp.2018.10.019.

[12] V. Kocaba, E. Gallucci, K.L. Scrivener, Methods for determination of degree of reaction of slag in blended cement pastes, Cem. Concr. Res. 42 (2012) 511–525, https://doi.org/10.1016/j.cemconres.2011.11.010.

[13] S.S. Bangaru, C. Wang, M. Hassan, H.W. Jeon, T. Ayiluri, Estimation of the degree of hydration of concrete through automated machine learning based microstructure analysis – A study on effect of image magnification, Adv. Eng. Inf. 42 (2019) 100975, https://doi.org/10.1016/j.aei.2019.100975.

[14] F. Georget, W. Wilson, K.L. Scrivener, edxia: microstructure characterisation from quantified SEM-EDS hypermaps, Cem. Concr. Res. 141 (2021) 106327, https://doi.org/10.1016/j.cemconres.2020.106327.

[15] F. Zunino, K. Scrivener, Microstructural developments of limestone calcined clay cement (LC3) pastes after long-term (3 years) hydration, Cem. Concr. Res. 153 (2022) 106693, https://doi.org/10.1016/j.cemconres.2021.106693.

[16] G. Constantinides, F.-J. Ulm, K. Van Vliet, On the use of nanoindentation for cementitious materials, Mat. Struct. 36 (2003) 191–196, https://doi.org/10/ffkbhj.

[17] G. Constantinides, K.S. Ravi Chandran, F.-J. Ulm, K.j., Van Vliet, Grid indentation analysis of composite microstructure and mechanics: Principles and validation, Materials Science and Engineering: A 430 (2006) 189–202, https://doi.org/10.1016/j.msea.2006.05.125.

[18] P. Lura, P. Trtik, B. Münch, Validity of recent approaches for statistical nanoindentation of cement pastes, Cem. Concr. Compos. 33 (2011) 457–465, https://doi.org/10/cbnjk3.

[19] Z. Luo, W. Li, Y. Gan, K. Mendu, S.P. Shah, Applying grid nanoindentation and maximum likelihood estimation for N-A-S-H gel in geopolymer paste: Investigation and discussion, Cem. Concr. Res. 135 (2020) 106112, https://doi.org/10.1016/j.cemconres.2020.106112.

[20] K.J. Krakowiak, J.J. Thomas, S. Musso, S. James, A.-T. Akono, F.-J. Ulm, Nano-chemo-mechanical signature of conventional oil-well cement systems: Effects of elevated temperature and curing time, Cem. Concr. Res. 67 (2015) 103–121, https://doi.org/10.1016/j.cemconres.2014.08.008.

[21] Z. Zhang, J. Qin, Z. Ma, X. Pang, Y. Zhou, Comparison of three different deconvolution methods for analyzing nanoindentation test data of hydrated cement paste, Cem. Concr. Compos. (2023) 104990, https://doi.org/10.1016/j.cemconcomp.2023.104990.

[22] Y. Chang, M. Lin, U. Hangen, S. Richter, C. Haase, W. Bleck, Revealing the relation between microstructural heterogeneities and local mechanical properties of complex-phase steel by correlative electron microscopy and nanoindentation characterization, Mater. Des. 203 (2021) 109620, https://doi.org/10.1016/j.matdes.2021.109620.

[23] F. Bruno, G. Konstantopoulos, G. Fiore, E. Rossi, M. Sebastiani, C. Charitidis, L. Belforte, M. Palumbo, A novel machine learning method to exploit EBSD and nanoindentation for TRIP steels microstructures analysis, Mater. Des. 239 (2024) 112774, https://doi.org/10.1016/j.matdes.2024.112774.

[24] J.J. Chen, L. Sorelli, M. Vandamme, F.-J. Ulm, G. Chanvillard, A coupled nanoindentation/SEM-EDS study on low water/cement ratio portland cement paste: evidence for C–S–H/Ca(OH)2 nanocomposites, J. Am. Ceram. Soc. 93 (2010) 1484–1493, https://doi.org/10.1111/j.1551-2916.2009.03599.x.

[25] W. Wilson, J.M. Rivera-Torres, L. Sorelli, A. Durán-Herrera, A. Tagnit-Hamou, The micromechanical signature of high-volume natural pozzolan concrete by combined statistical nanoindentation and SEM-EDS analyses, Cem. Concr. Res. 91 (2017) 1–12, https://doi.org/10.1016/j.cemconres.2016.10.004.

[26] Y. Abdallah, M. Vandamme, C. Chateau, D. Garnier, I. Jolivet, A. Onaisi, D. Richard, S. Zandi, Linking elastic properties of various carbonate rocks to their microstructure by coupling nanoindentation and SEM-EDS, Int. J. Rock Mech. Min. Sci. 170 (2023) 105456, https://doi.org/10.1016/j.ijrmms.2023.105456.

[27] Y. Wei, A combined SPM/NI/EDS method to quantify properties of inner and outer C-S-H in OPC and slag-blended cement pastes, Cem. Concr. Compos. (2018) 11, https://doi.org/10/ghdf8c.

[28] B. Hilloulin, M. Robira, A. Loukili, Coupling statistical indentation and microscopy to evaluate micromechanical properties of materials: Application to viscoelastic behavior of irradiated mortars, Cem. Concr. Compos. 94 (2018) 153–165, https://doi.org/10/ghdf49.

[29] M. Schwaighofer, L. Zelaya-Lainez, M. Königsberger, M. Lukacevic, S. Serna-Loaiza, M. Harasek, O. Lahayne, V. Senk, J. Füssl, Characterization of mechanical properties of five hot-pressed lignins extracted from different feedstocks by microscopy-aided nanoindentation, Mater. Des. 227 (2023) 111765, https://doi.org/10.1016/j.matdes.2023.111765.

[30] J.J. Hughes, P. Trtik, Micro-mechanical properties of cement paste measured by depth-sensing nanoindentation: a preliminary correlation of physical properties with phase type, Mater Charact 53 (2004) 223–231, https://doi.org/10/cqbg8q.

[31] C. Hu, Z. Li, Micromechanical investigation of Portland cement paste, Constr. Build. Mater. 71 (2014) 44–52, https://doi.org/10.1016/j.conbuildmat.2014.08.017.

[32] Y. Gan, M. Vandamme, H. Zhang, Y. Chen, E. Schlangen, K. Van Breugel, B. Šavija, Micro-cantilever testing on the short-term creep behaviour of cement paste at micro-scale, Cem. Concr. Res. 134 (2020) 106105, https://doi.org/10.1016/j.cemconres.2020.106105.

[33] W. Guo, Y. Wei, Investigation of compressive creep of calcium-silicate-hydrates (C-S-H) in hardened cement paste through micropillar testing, Cem. Concr. Res. 177 (2024) 107427, https://doi.org/10.1016/j.cemconres.2024.107427.
[34] X. Su, Y. Wu, M. Jia, Z. Liu, J. Jiang, W. Xu, Multiscale creep model for concrete considering from C-S-H gel scale to mesoscale with ITZ and irregular-shaped aggregates, Cem. Concr. Compos. 143 (2023) 105254, https://doi.org/10.1016/j.cemconcomp.2023.105254.
[35] X. Su, M. Jia, Y. Wu, L. Yao, W. Xu, A hierarchical creep model for cement paste: From decoding nano-microscopic C-S-H creep to considering microstructure evolution, Journal of Building Engineering 78 (2023) 107606, https://doi.org/10.1016/j.jobe.2023.107606.
[36] Y. Liu, Y. Li, C. Jin, H. Li, Multi-scale creep analysis of cement paste – Indentation prediction and time correspondence of mechanisms, Cem. Concr. Compos. 134 (2022) 104815, https://doi.org/10.1016/j.cemconcomp.2022.104815.
[37] Y. Li, Y. Liu, Z. Wang, H. Li, J. Mu, Effect of phases on the creep properties of cement paste based on indentation test and homogenization scheme, Constr. Build. Mater. 317 (2022) 125957, https://doi.org/10.1016/j.conbuildmat.2021.125957.
[38] Y. Li, Y. Liu, Y. Li, Y. Li, R. Wang, Evaluation of concrete creep properties based on indentation test and multiscale homogenization method, Cem. Concr. Compos. 123 (2021) 104135, https://doi.org/10.1016/j.cemconcomp.2021.104135.
[39] J. Frech-Baronet, L. Sorelli, J.-P. Charron, New evidences on the effect of the internal relative humidity on the creep and relaxation behaviour of a cement paste by micro-indentation techniques, Cem. Concr. Res. 91 (2017) 39–51, https://doi.org/10/f9hpsq.
[40] H.M. Jennings, J.J. Thomas, J.S. Gevrenov, G. Constantinides, F.-J. Ulm, Nanostructure of C-S-H gel in cement paste as a function of curing conditions and relative humidity, (n.d.) 20.
[41] P. Suwanmaneechot, A. Aili, I. Maruyama, Creep behavior of C-S-H under different drying relative humidities: Interpretation of microindentation tests and sorption measurements by multi-scale analysis, Cem. Concr. Res. 132 (2020) 106036, https://doi.org/10.1016/j.cemconres.2020.106036.
[42] M. Vandamme, Q. Zhang, F.-J. Ulm, R. Le Roy, B. Zuber, E. Gartner, P. Termkhajornkit, Creep Properties of Cementitious Materials from Indentation Testing: Significance, Influence of Relative Humidity, and Analogy Between C-S-H and Soils, (2013) 48–61. https://doi.org/10.1061/9780784413111.005.
[43] Z. Chen, L. Sorelli, Effect of relative humidity and porosity on the logarithmic creep of the layered C–S–H minerals tobermorite and jennite, Cem. Concr. Compos. 116 (2021) 103872, https://doi.org/10.1016/j.cemconcomp.2020.103872.
[44] B.K. Marsh, R.L. Day, Pozzolanic and cementitious reactions of fly ash in blended cement pastes, Cem. Concr. Res. 18 (1988) 301–310, https://doi.org/10.1016/0008-8846(88)90014-2.
[45] K. Scrivener, R. Snellings, B. Lothenbach, A practical guide to microstructural analysis, 2015.
[46] T.J. Collins, ImageJ for microscopy, Biotechniques 43 (2007) S25–S30, https://doi.org/10.2144/000112517.
[47] W. Wilson, L. Sorelli, A. Tagnit-Hamou, Automated coupling of nanoindentation and quantitative energy-dispersive spectroscopy (NI-QEDS): A comprehensive method to disclose the micro-chemo-mechanical properties of cement pastes, Cem. Concr. Res. 103 (2018) 49–65, https://doi.org/10.1016/j.cemconres.2017.08.016.
[48] K.J. Krakowiak, W. Wilson, S. James, S. Musso, F.-J. Ulm, Inference of the phase-to-mechanical property link via coupled X-ray spectrometry and indentation analysis: Application to cement-based materials, Cem. Concr. Res. 67 (2015) 271–285, https://doi.org/10.1016/j.cemconres.2014.09.001.
[49] W.C. Oliver, G.M. Pharr, An improved technique for determining hardness and elastic modulus using load and displacement sensing indentation experiments, J. Mater. Res. 7 (1992) 1564–1583, https://doi.org/10/bdv47f.
[50] G. Constantinides, F.-J. Ulm, The effect of two types of C-S-H on the elasticity of cement-based materials: Results from nanoindentation and micromechanical modeling, Cem. Concr. Res. 34 (2004) 67–80, https://doi.org/10.1016/S0008-8846(03)00230-8.
[51] M. Vandamme, F.-J. Ulm, Nanoindentation investigation of creep properties of calcium silicate hydrates, Cem. Concr. Res. 52 (2013) 38–52, https://doi.org/10/f5f4zk.
[52] Q. Zhang, R. Le Roy, M. Vandamme, B. Zuber, Long-term creep properties of cementitious materials: comparing microindentation testing with macroscopic uniaxial compressive testing, Cem. Concr. Res. 58 (2014) 89–98, https://doi.org/10.1016/j.cemconres.2014.01.004.
[53] I. Bekrine, B. Hilloulin, A. Loukili, Multiscale investigation of cement pastes with low and high-grade calcined clays and slag at early and advanced ages, Journal of Building Engineering (2023) 107570, https://doi.org/10.1016/j.jobe.2023.107570.
[54] Y. Wei, X. Gao, S. Liang, Nanoindentation-based study of the micro-mechanical properties, structure, and hydration degree of slag-blended cementitious materials, J Mater Sci 51 (2016) 3349–3361, https://doi.org/10.1007/s10853-015-9650-4.
[55] D. Tavakoli, A. Tarighat, Molecular dynamics study on the mechanical properties of Portland cement clinker phases, Comput. Mater. Sci 119 (2016) 65–73, https://doi.org/10.1016/j.commatsci.2016.03.043.
[56] I. Bekrine, B. Hilloulin, A. Loukili, in: Micromechanical Properties Assessment of Slag Blended Cements Using Nanoindentation and Scanning Electron Microscopy, Springer Nature, Switzerland, Cham, 2023, pp. 88–98, https://doi.org/10.1007/978-3-031-33187-9_9.
[57] M. Vandamme, F.-J. Ulm, Nanogranular origin of concrete creep, Proceedings of the National Academy of Sciences 106 (2009) 10552–10557. https://doi.org/10/dfs8nq.
[58] I.O. Yaman, N. Hearn, H.M. Aktan, Active and non-active porosity in concrete Part I: Experimental evidence, Mat. Struct. 35 (2002) 102–109, https://doi.org/10.1007/BF02482109.
[59] O. Bernard, F.-J. Ulm, E. Lemarchand, A multiscale micromechanics-hydration model for the early-age elastic properties of cement-based materials, Cem. Concr. Res. 33 (2003) 1293–1309, https://doi.org/10.1016/S0008-8846(03)00039-5.
[60] S. Liang, Y. Wei, Effects of water-to-cement ratio and curing age on microscopic creep and creep recovery of hardened cement pastes by microindentation, Cem. Concr. Compos. 113 (2020) 103619, https://doi.org/10.1016/j.cemconcomp.2020.103619.
[61] R. Le Roy, Déformations instantanées et différées des bétons à hautes performances, Ecole Nationale Des Ponts et Chaussées (1995).